

Cortical Mapping of Callosal Connections in Healthy Young Adults

Yirong Xiong¹, Liyuan Yang¹, Changtong Wang¹, Chenxi Zhao¹, Junhao Luo¹, Di Wu¹, Yiping Ouyang², Michel Thiebaut de Schotten^{3,4}, and Gaolang Gong^{1,5,6,✉}

¹State Key Laboratory of Cognitive Neuroscience and Learning & IDG McGovern Institute for Brain Research, Beijing Normal University, Beijing, China

²The Queen's University of Belfast Joint College, China Medical University, Shenyang, China

³Brain Connectivity and Behaviour Laboratory, Sorbonne Université, Paris, France

⁴Groupe d'Imagerie Neurofonctionnelle, Institut des Maladies Neurodégénératives-UMR 5293, Centre National de la Recherche Scientifique, Commissariat à l'Energie Atomique, University of Bordeaux, Bordeaux, France

⁵Beijing Key Laboratory of Brain Imaging and Connectomics, Beijing Normal University, Beijing, China

⁶Chinese Institute for Brain Research, Beijing, China

The corpus callosum (CC) is the principal white matter (WM) bundle supporting communication between the two brain hemispheres. Despite its importance, a comprehensive mapping of callosal connections is still lacking. Here, we constructed the first bidirectional population-based callosal connectional atlas between the midsagittal section of the CC and the cerebral cortex of the human brain by means of diffusion-weighted imaging tractography. The estimated connectional topographic maps within this atlas have the most fine-grained spatial resolution, demonstrate histological validity, and were reproducible in two independent samples. This new resource, a complete and comprehensive atlas, will facilitate the investigation of interhemispheric communication and come with a user-friendly companion online tool ([CCmapping](#)) for easy access and visualization of the atlas.

Corpus callosum | Cerebral cortex | Cortical topography | Callosal connection | Diffusion MRI

Correspondence: gaolang.gong@bnu.edu.cn

Introduction

The corpus callosum (CC) is the major white matter (WM), integrating information and coordinating cognitive processing between the two cerebral hemispheres⁽¹⁾. The midsagittal section of the corpus callosum (mCC) is usually preferred to measure this prominent fiber bundle in postmortem brain samples or in vivo magnetic resonance images for simplicity, as it summarizes the properties of all callosal fibers. Various mCC measures (e.g., morphology and diffusivity parameters) have shown significant correlations with biological factors (e.g., age and sex), cognitions, and brain diseases^(2–5). Mapping detailed connections between the mCC and cortical regions is fundamental for investigating and understanding interhemispheric communication. Knowing what mCC regions are connected to is critical to understanding their functions. Numerous studies have reported significant group dif-

ferences in various regions of the mCC^(4, 6–8). For each reported cluster or region on the mCC, it is always necessary to interpret its functional relevance. To achieve this, previous studies typically mapped the observed mCC clusters or regions onto the mCC subdivisions (e.g., genu, body, and splenium) and referred to existing connectional topographies of mCC^(9, 10). Therefore, the accuracy and reliability of research results are largely dependent on the choice of mapping and the quality of the topographies used.

Mapping of the human corpus callosum can be achieved using three approaches: chemical tracing^(11–17), lesion studies⁽¹⁸⁾, and diffusion MRI (dMRI) techniques^(10, 19, 20). Chemical tracing is not feasible for the human brain due to their invasive nature. Correlating focal cortical lesions with Wallerian degeneration in the mCC was also applied to achieve such mapping. However, this type of *in vitro* method is not comprehensive and requires postmortem lesioned-brain. The third approach is diffusion MRI techniques, which have been used noninvasively to map human CC connections *in vivo*. Specifically, the callosal fibers passing through the mCC were virtually reconstructed as streamlines using diffusion MRI tractography. In so doing, mCC voxels were directly associated with cortical regions. Such approaches are more commendable than others, such as the geometrical parcellation of the mCC⁽⁹⁾ only have an approximate relationship with cortical regions. A few studies also applied this approach to obtain topographic maps of the mCC for particular cortical regions that were defined anatomically^(21–23) or functionally^(24–26). These studies proved the feasibility of diffusion MRI tractography-based mapping for human brain callosal connections. They are, however, limited by only partial topographic mapping, old-fashioned diffusion MRI acquisition and tractography algorithms, and a very small number of scanned subjects.

More importantly, these mappings suffer from two significant limitations: firstly, the qualitative nature of the summarized topographies for each mCC subdivision often results in a lack of a clearly defined boundary on the cortical surface, and secondly, due to their fixed parcellation of mCC, clusters or regions located within the same subdivision may share similar inferred topographies, regardless of their size or location.

The present study constructed a comprehensive population-based human brain callosal atlas containing detailed connectional topographies between mCC voxels and cortical regions. The notably high-quality diffusion MRI datasets from the ~1000 Human Connectome Project (HCP) healthy young adults, together with well-refined diffusion MRI tractography, were used to virtually reconstruct callosal fibers (Fig. 1)⁽²⁷⁾. For each mCC voxel, two weighted cortical connectional topographic maps were generated at the population level; for each pair of homotopic cortical regions, two weighted mCC connectional topographic maps were generated at the population level. Furthermore, we developed an online tool to 1) interactively visualize such a comprehensive atlas and 2) estimate cortical or mCC topographic maps for customized mCC or cortical regions of interest (ROIs).

Materials and Methods

MRI dataset. The dataset included all possible HCP participants for whom both diffusion and T1 images were available (27). It comprised 928 healthy young adults (female/male: 503/425; age range: 22–37 years; 846 right-handed). The exclusion criteria of HCP participant recruitment included severe neurodevelopmental disorders (such as autism), neuropsychiatric disorders (like schizophrenia or depression), neurological disorders (e.g., Parkinson’s disease), or chronic illnesses (such as diabetes or high blood pressure). Twins born before 34 weeks of gestation and non-twins born before 37 weeks were excluded due to the increased risks associated with prematurity. The detailed information regarding the HCP participants’ socio-economic status, substance use, intelligence, and sibship are included in the Supplementary Materials.

Informed consent was obtained from all subjects, and the protocol was approved by the Institutional Review Board of Washington University. MRI scanning was performed using a customized Siemens Connectome Skyra 3T scanner. Diffusion-weighted (DW) images were acquired using a spin-echo echo-planar imaging (EPI) sequence with the following parameters: repetition time (TR) = 5520 ms, echo time (TE) = 89.5 ms, flip angle = 78°, FOV = 210 × 180 mm², matrix = 168 × 144, slices = 111, and resolution = 1.25 mm × 1.25 mm × 1.25 mm. Diffusion weightings of b = 0, 1000, 2000, and 3000 s/mm² were applied in the 18, 90, 90 and 90 directions, respectively. High-resolution 3D T1-weighted (T1W) images were acquired using a magnetization prepared rapid gradient echo (MPRAGE) sequence using the following parameters: TR = 2400 ms, TE = 2.14 ms, TI = 1000 ms, flip angle = 8°, FOV = 224 × 224 mm², and resolution = 0.7 mm × 0.7 mm × 0.7 mm. DW and T1W images were preprocessed using the HCP minimal preprocessing pipeline (28).

Individual midsagittal CC (mCC) and its alignment to the template.

The HCP minimal preprocessing pipeline aligned the anterior commissure (AC), the AC–posterior commissure (PC) line, and the interhemispheric plane of the T1W images to the MNI template using a rigid transform of 6 degrees of freedom. This transformation maintains the original size and shape of the brain. On the resultant T1W image of each individual, the midsagittal plane slice was selected, and the mCC boundary was then manually outlined by a trained rater (D.W.). The mCC boundary of 50 randomly selected participants was outlined two weeks later by the rater to assess the manual outlining reliability. The Dice coefficient of the mCC masks ranged from 0.95 to 0.99 (mean: 0.98, SD: 0.009), and the intraclass correlation coefficient (ICC) of the mCC area reached 0.99.

To ensure voxel-wise comparability across individuals, the individual mCC was nonlinearly aligned to a manually outlined template mCC on the MNI152 template image (29). Specifically, the 2D sagittal image of the template mCC was set as the target image (or the fixed image), and the 2D sagittal image of the individual mCC was set as the source im-

age (or the moving image). The two 2D images were first smoothed with a 2D Gaussian smoothing kernel (σ = 1) by using the ‘imGaussfilt’ function in MATLAB. Next, we linearly aligned the source image to the target image (i.e., performed a 2D affine transform of 8 degrees of freedom, including translation, rotation, scaling, and shearing) using the ‘imregtform’ function in MATLAB. Next, we performed nonlinear registration from the linearly aligned source image to the target image using the demons algorithm that was implemented by the ‘imregdemons’ function in MATLAB. Here, three multiresolution image pyramid levels were used, and 100 iterations were estimated at each pyramid level. Gaussian smoothing (σ = 1) was applied to regularize the accumulated displacement field at each iteration. To maximize the aligning accuracy, this whole nonlinear registration procedure was iterated 5 times. Finally, the linear and nonlinear displacement fields were merged, and this merged field can be used to transform the individual mCC into the template space. For each individual, the mCC alignment was carefully checked by visual inspection.

Callosal fiber tracking with diffusion MRI-based tractography.

For each subject, diffusion MRI-based tractography was used to extract callosal fiber streamlines that passed through the individual mCC above. Specifically, fiber orientation distributions (FODs) of each voxel were first estimated using multi-shell, multi-tissue constrained spherical deconvolution with a harmonic order of 8 and default parameters using Mrtrix3 (30, 31). Probabilistic fiber tracking was then performed using the 2nd-order integration over FODs (iFOD2) algorithm in Mrtrix3 (32). Given our focus on the callosal fibers, the mCC was set as an inclusion mask (i.e., saving only fibers traversing the mCC) in fiber tracking. Due to the ambiguous existence of callosal fibers connecting bilateral subcortical nuclei, all subcortical nuclei were set as exclusion masks (i.e., fibers traversing them were discarded). Here, subcortical nuclei, including the thalamus, hippocampus, amygdala, caudate, putamen, pallidum, and accumbens, were extracted using the FIRST tool of the FMRIB Software Library (FSL) (33). To improve the biological accuracy of the tractograms, the anatomically constrained tractography (ACT) framework was used, which incorporates prior anatomical information into the tractography (34). The anatomical information was obtained by segmenting T1W images into tissue partial volume maps (PVMs) for WM, GM, and cerebrospinal fluid (CSF) using FSL tools. The resultant PVM images were then taken as anatomical priors into the ACT framework. For each HCP participant, the minimal preprocessed T1W image was well aligned with the DW images; therefore, the mCC and PVM images were already in the DW image space. The detailed fiber-tracking parameters were as follows: step size = 0.625 mm (default), maximum curvature per step = 45°, FOD threshold = 0.05, and length range = 2.5–250 mm. For each subject, 10 million streamlines were generated by seeding from and ending into the ACT-generated GM-WM interface (GMWMI) (Fig. 1).

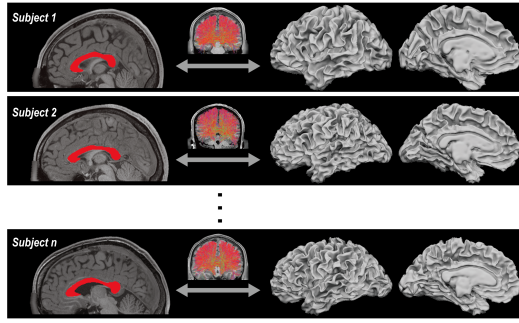


Fig. 1. Schematics of estimating individual-level callosal connections between the mCC and cortical regions on the white surface via diffusion MRI-based fiber tracking. For selected individuals, the mCC mask (left), callosal fibers (middle), and cortical white surface (right) were displayed.

Mapping cortical topography for mCC voxels. For each streamline, the passing coordinate was first estimated on the individual mCC and then transformed onto the template mCC of the MNI space using the spatial alignment of the mCC above. All passing streamlines therefore could be determined for each voxel or a cluster of voxels on the template mCC.

For each HCP subject, the minimal preprocessing pipeline provides FreeSurfer-generated individual pial and white surfaces resampled onto the standard *32k_fs_LR* mesh (containing 32k vertices for each hemispheric surface). For each streamline, its connected cortical vertex was determined as the closest vertex on the white surface within a sphere with a 2-mm radius centered at its endpoint (one in each hemisphere). We excluded the streamlines that failed to find any vertex within a sphere within a 2-mm radius centered at its endpoint. In average, 4.67 million streamlines were excluded at the subject level.

For each voxel of the template mCC (1554 voxels in total), a cortical *32k_fs_LR* surface map of streamline count (i.e., connectional topography) was then derived for each subject using all passing streamlines. At the group level, we adopted two weighting schemes for such connectional topographic maps: populational probability (PP) and normalized streamline number (NSN). Briefly, the PP map represented the incidence of finding certain callosal connections across young adult population. On the other hand, the NSN map reflected the averaged density/strength of certain callosal connections across young adult population. These two maps would provide complementary measures for each callosal connections of interests. Specifically, for the PP-weighted topographic map, we first binarized the individual maps of streamline count and later calculated a probability map across all individuals. For the NSN-weighted topographic map, we normalized the individual maps of streamline count by scaling the total number of all included callosal streamlines of each subject to 5 million and then averaged across all subjects. Specifically, because the streamline number scaling across different voxels is uniform, it enables additivity and comparability among different NSN maps.

In addition, we applied the same strategies discussed above to estimate cortical connectional topographies for mCC subparts that were derived from three influential parcellations of

mCC: the Witelson (6 mCC subdivisions) (9), Aboitiz (10 mCC subdivisions) (35), and Hofer (5 mCC subdivisions) parcellations (10).

Mapping mCC topography for homotopic cortical regions. Notably, most but not all callosal fibers connect homotopic cortical regions, but we here only constructed mCC topography for homotopic cortical regions for simplicity. Specifically, we applied several widely used atlases to parcellate the entire cortical surface into cortical regions at different spatial resolutions: ~100 regions, ~200 regions, and ~500 regions within each hemisphere. The first is the Brainnetome atlas (BNA), which was derived from WM connectional information (36). It includes 105 cerebral cortical regions in each hemisphere. The second is HCP multimodal parcellation (HCPMMP), which is based on multiple neurobiological properties (37). It includes 180 cerebral cortical regions in each hemisphere. In these two parcellation schemes, cortical regions are homotopically paired between the two hemispheres. The other two parcellations are from the 1000-Parcels version of the Schaefer2018 Parcellation that was based on resting-state functional connectional information (38). It includes 500 and 498 cerebral cortical regions in the left and right hemispheres, respectively, and these regions are not homotopic between the two hemispheres. We therefore mirrored the parcellation of each hemisphere to the opposite hemisphere, resulting in two symmetric parcellations: Schaefer_L and Schaefer_R.

For each pair of homotopic cortical regions, all connected streamlines and their passing voxels on the template mCC can be determined. Accordingly, a streamline count map of template mCC (i.e., connectional topography) was derived for each subject. At the population level, we also generated two topographic maps, the PP-weighted and NSN-weighted maps, for each pair of homotopic cortical regions.

Reproducibility analysis. To test the sampling effect on our currently observed population-based topographic maps, we re-estimated topographic maps with split-half HCP samples (464 HCP subjects for each sample) and assessed the similarities of resultant topographic maps between the two split-half samples. Next, to evaluate the sibling confounding effects on the maps, we re-estimated the topographic maps using the 93 unrelated (nonsibling) subjects from the HCP unrelated set and evaluated their similarities with the main maps. Finally, a larger number of initially generated callosal streamlines from tractography is preferred for estimating stable topographic maps. However, an excessively large number comes with a very large burden of data storage and computation. To assess whether the 10 M initially generated callosal streamlines from tractography for our main analysis was enough, we compared the topographic maps between our main scheme (i.e., 10 M streamlines) and validation schemes (i.e., from 13 M to 22 M streamlines) using the unrelated HCP subjects. For either cortical topographic maps or mCC topographic maps, both the Pearson correlation coefficient (*R*) and intraclass correlation coefficient (*ICC*) were used to quantify the degree of similarities between the two

topographic maps.

Thresholding topographic maps. To determine a practically meaningful boundary for each population-based topographic map, we applied a permutation procedure and estimated a cutoff value at the statistically significant level of $p = .05$. Here, we take the population-based cortical topographic map for a mCC voxel/subpart as an example. For each subject, we first permuted the values on the individual-based topographic map by adopting Moran spectral randomization, which preserves the spatial autocorrelation of the map (39). Using the resultant permuted individual-based maps, we then generated a randomized population-based topographic map with different resolutions and different weighting schemes, as described above. We repeated the same procedure 10000 times, resulting in 10000 randomized population-based topographic maps. The 95th percentiles of maximal values in the 10000 randomized population-based maps were calculated as the cutoff value, which corresponds to the statistical significance level $p = .05$ for weight values within the topographic map. Likewise, for each homotopic cortical regional pair, the cutoff value for its population-based topographic mCC map was estimated using the same permutation procedure.

CCmapping: An online interactive viewer for both mCC and cortical topographic maps. We developed a web-based viewer using JavaScript to interactively visualize each population-based topographic map above. This tool was largely based on the open-source library BrainBrowser (40). BrainBrowser supports real-time visualization of the 3D cortical surface, brain volume, and various kinds of neuroimaging data in any modern web browser by WebGL, HTML5, and other technologies. In addition, Echarts and Node.js technologies were applied.

Application of mCC and cortical topographic maps. High-resolution connectional topographic maps are essential for CC studies, particularly those concerning the relationship between callosal fibers and connected cortical regions. As examples, we applied the estimated topographic maps above to perform two specific investigations as follows. Firstly, neural axons within the WM tract are segregated in an orderly manner according to their originating topographies (41). In line with this hypothesis, callosal axons originating from one dorsal region (i.e., M1) and another ventral region (i.e., S1) in mice showed strictly dependent dorsal and ventral positioning on the midline (42). However, it remains unclear whether such observed positional dependence can be generalized to the entire CC of the human brain. To answer this question, we conducted analyses as discussed further. For each voxel on the template mCC, we extracted its coordinate along the Z and Y axes. We extracted the barycenter coordinates of the connected cortical region of each voxel (derived from the thresholded cortical topographic map at $p = .05$) along the Z and Y axes. Here, the Z and Y coordinates represent relative positioning along the dorsal-ventral (D-V) and anterior-posterior (A-P) axes within the human brain, respectively.

Pearson correlation between the two Z or Y coordinates was then evaluated across all mCC voxels. A significant Z or Y coordinate correlation indicates a D-V or A-P positional dependence between the callosal axon and the connected cortical regions across the entire CC.

Secondly, cortical myelin content and callosal fiber composition exhibit significant variation across the entire cortex and mCC, respectively. Recent studies found that cortical myelin content was correlated with callosal fiber length scaling. This suggests a biological link between cortical myeloarchitecture and the efficacy of cortical communication to the contralateral hemisphere (29). To further determine whether the myelin content of parcellated cortical regions relates to the composition of their connected callosal fibers, we conducted the analyses discussed above. We quantified cortical myelin content by adopting the HCP group-averaged T1w/T2w values on the standard 32k_fs_LR surface (43). Similarly, we quantified callosal fiber composition by adopting the HCP group-averaged values of two dMRI-derived parameters on the template mCC: neurite density index (NDI) and orientation dispersion index (ODI) (44). For each pair of homotopic regions from the 4 cortical parcellations above (i.e., BNA, HCPMP, Schaefer_L/Schaefer_R), the regional mean T1w/T2w ratio value was calculated and then averaged between the left and right regions; for the passing mCC region of each homotopic region pair (derived from the thresholded mCC topographic map at $p = .05$), the mean NDI and ODI values were calculated. For each cortical parcellation, Pearson correlation between the T1/T2 ratio and NDI or ODI values was then evaluated across all cortical regional pairs.

Results

Cortical topographic maps for mCC voxels and subdivisions. For each cortical topographic map, a cutoff value for the PP or NSNweights was estimated at the statistical significance level of $p < .05$. In Fig. 2A, we show both non-thresholded and thresholded PP-weighted topographic maps for 10 selected voxels that are approximately evenly distributed across the template mCC. In addition, Fig. 2B-D shows the PP-weighted topographic maps for each mCC subdivision from the well-known Abotiz (35), Witelson (9), and Hofer parcellation (10). The NSN-weighted topographic maps for these selected mCC voxels or subdivisions are illustrated in Fig. S1, and their spatial patterns are similar to the PP-weighted ones. The topographic maps for all mCC voxels and subdivisions can be easily viewed and accessed via *CCmapping*.

As shown, the estimated cortical topographic maps are highly compatible with prior information in neuroanatomy. The voxels and subdivisions in the most anterior mCC part (e.g., genu) mainly contain callosal streamlines projecting to the prefrontal cortex. The anterior and middle parts of the mCC mainly contain callosal streamlines projecting to the premotor and supplementary motor areas. The most posterior part of the mCC contains callosal streamlines projecting to the parietal, temporal, and occipital cortices.

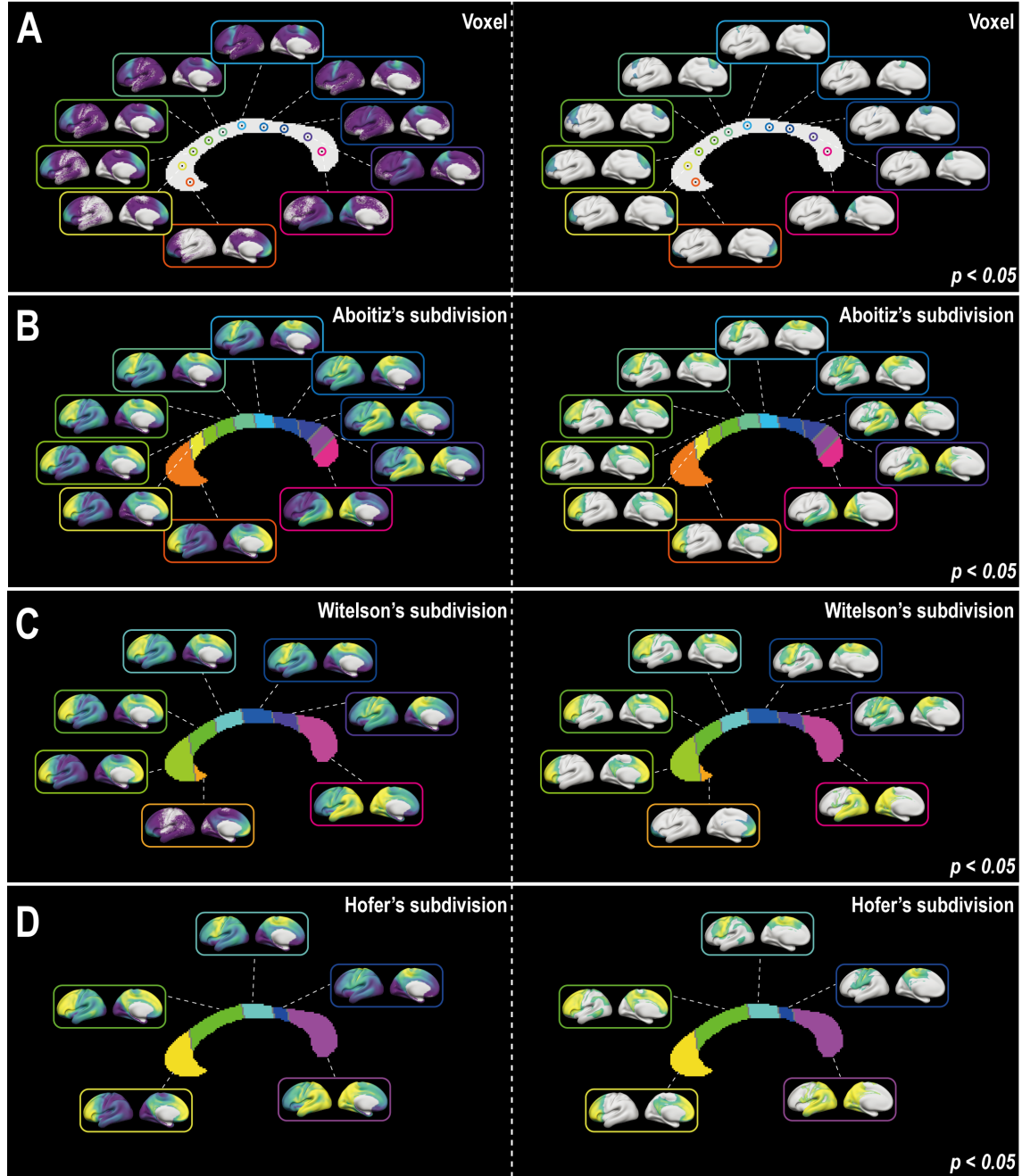


Fig. 2. Population-based probability-weighted cortical topographies for mCC voxels and subdivisions. (A) Cortical topographic maps for 10 selected voxels on the mCC. Each voxel is indicated by a small circle. (B) Cortical topographic maps for the 10 mCC subdivisions from the Aboitiz parcellation (35). (C) Cortical topographic maps for the 7 mCC subdivisions from the Witelson parcellation (9). (D) Cortical topographic maps for the 5 mCC subdivisions from the Hofer parcellation (10). The nonthresholded and thresholded (i.e., $p < .05$) maps are illustrated in the left and right panels, respectively.

mCC topographic maps for homotopic cortical regional pairs. For each homotopic regional pair, PP-weighted and NSN-weighted mCC topographic maps were generated. For each mCC topographic map, a cutoff value for the PP or NSN-weights was also estimated at the statistical significance level of $p = .05$. For each parcellation scheme, we randomly selected six pairs of homotopic regions that were approximately evenly distributed across the frontal, parietal, temporal, and occipital cortices. Both non-thresholded and thresholded PP-weighted and NSN-weighted topographic maps were illustrated for the six pairs of homo-

topic regions (Fig. 3 and Fig. S2). Again, the topographic maps for all pairs of homotopic regions can be easily viewed, and accessed via CCmapping.

In concordance with prior information in neuroanatomy, callosal streamlines connecting bilateral prefrontal cortices mainly pass through the very anterior part of the mCC. Callosal streamlines connecting the bilateral premotor and motor cortices mainly pass through the anterior and middle parts of the mCC. Callosal streamlines connecting the bilateral parietal, temporal, and occipital cortices mainly pass through the posterior parts of the mCC.

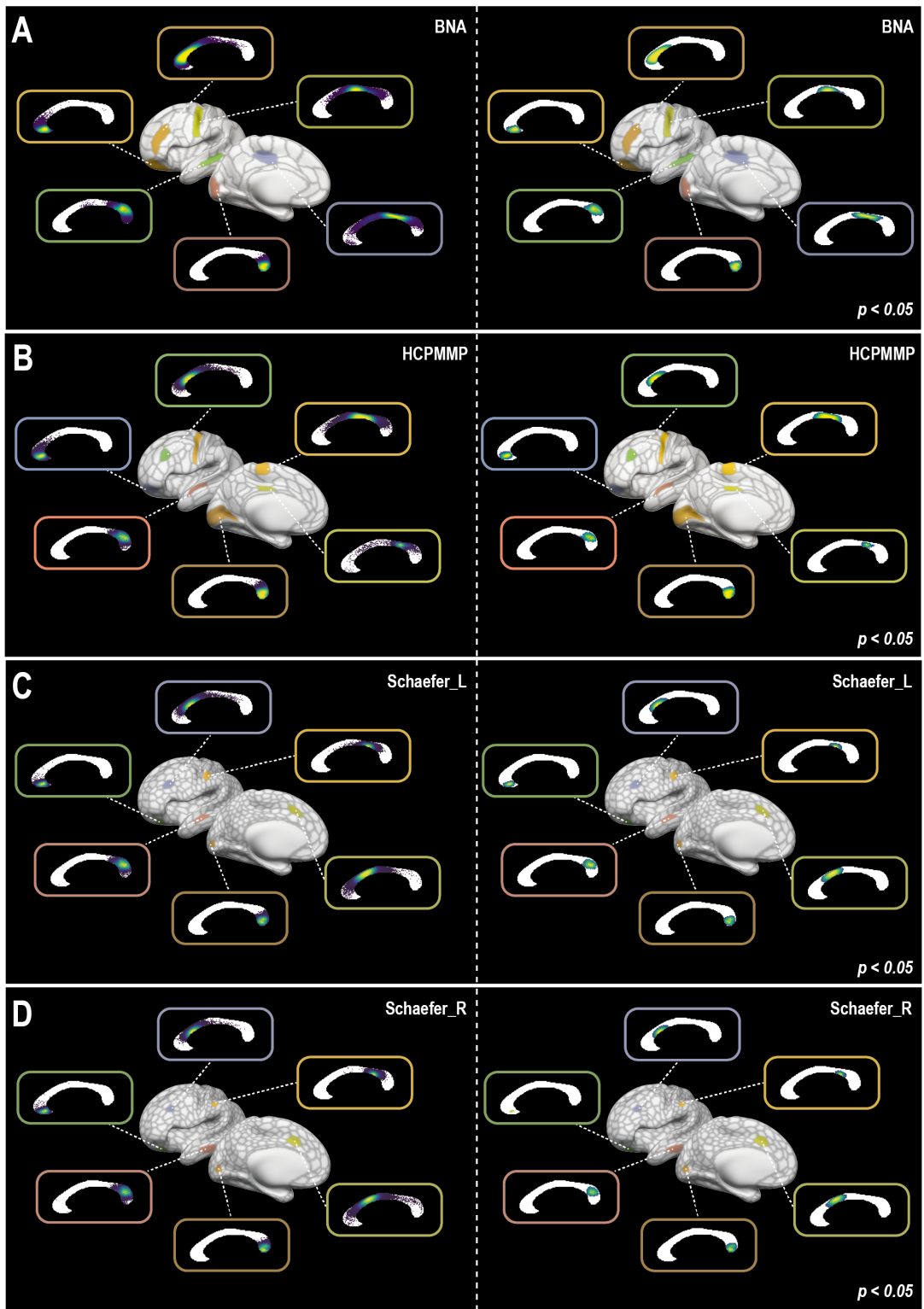


Fig. 3. Population-based probability-weighted mCC topographies for homotopic cortical regional pairs. (A) mCC topographic maps for 6 selected homotopic cortical regional pairs from the BNA (36). The selected regions are indicated by specific colors on the cortical surface. (B) mCC topographic maps for 6 selected homotopic cortical regional pairs from the HCPMMP (37). The selected regions are indicated by specific colors on the cortical surface. (C) mCC topographic maps for 6 selected homotopic cortical regional pairs from the Schaefer_L parcellation (38). (D) mCC topographic maps for 6 selected homotopic cortical regional pairs from the Schaefer_R parcellation. The nonthresholded and thresholded (i.e., $p < .05$) maps are illustrated in the left and right panels, respectively.

Validity and reproducibility. To evaluate the validity of our estimated topographic maps, we summarized the histological results of mapping the monkey or human brain between the mCC and cortical regions in the literature (Table 1). Specifically, we used the *CCmapping* to locate the most matched HCPMMP region or mCC subdivision for the injection site of the chemical tracer in each relevant study (8 in total). We then extracted the topographic maps from our atlas. As shown in Fig. S3:1-8, the comparison showed that our estimated topographies are highly consistent with previously reported histological data.

We evaluated the reproducibility of the estimated topographic maps for each mCC voxel or homotopic cortical regional pair by comparing the re-estimated topographic maps from two split-half HCP samples using Pearson correlation and intra-class correlation (ICC). As illustrated in Fig. 4 and Fig. S4, both Pearson correlation and ICC values are quite high (almost close to 1) for most mCC voxels. This indicates a high similarity of the cortical PP-weighted or NSN-weighted maps between the two split-half samples, suggesting a limited sampling effect on the results. Regarding the mCC topographic maps, most homotopic regional pairs showed high Pearson correlation and ICC values (almost close to 1). This demonstrates a high similarity of the resultant mCC PP-weighted or NSN-weighted maps between the two split-half samples. A few insular and temporal regions, however, showed medium and even low Pearson correlation and ICC values. Overall, the Schaefer_L/Schaefer_R parcellation has a lower Pearson correlation and ICC than the BNA and HCPMMP, suggesting a lower reproducibility of mCC topographic maps for higher spatial resolution of cortical parcellation. To evaluate the sibling effects on our results, we compared the topographic maps from the 93 unrelated HCP subjects with the main maps from the total HCP subjects. As shown in Fig. 4 and Fig S4, most Pearson correlations and ICCs are quite high. This indicates a high similarity of PP-weighted and NSN-weighted topographic maps between the unrelated and total HCP samples, indicating a limited sibling effect on our results. Finally, the resultant PP-weighted and NSN-weighted topographic maps estimated from more initially generated callosal streamlines have high similarity with our main results (i.e., from 10 M initially generated callosal streamlines). This shows a medium to high Pearson correlation and ICC values across mCC voxels and homotopic regional pairs (Fig. 5 and Fig. 5S). This shows that the 10 M initially generated callosal streamlines in our main analysis reached a stable estimation for these connectional topographic maps at the population level.

CCmapping: an online interactive viewer. We developed an online tool, i.e., *CCmapping*, to interactively visualize and export our generated mCC or cortical topographic maps. Fig. 6A illustrates the main interface for this tool. The left side of the interface, i.e., the mCC panel, supports 1) voxel or subdivision selection on the mCC while viewing cortical topographic maps and 2) visualization of mCC topographic maps after selecting a specific cortical region within the cortical surface panel on the right side. The right side of the inter-

face, i.e., the cortical surface panel, supports 1) region selection on the cortical surface while viewing mCC topographic maps and 2) visualization of cortical topographic maps after selecting a specific mCC voxel or subdivision within the mCC panel on the left side. The tool provides a set of statistics of the involved callosal streamlines (e.g., mean length, number, and connected cortical functions) in an embedded information box. All our estimated cortical or mCC topographic maps above are openly accessible through *CCmapping*. By default, after loading the requested mCC or cortical topographic map, *CCmapping* displays the thresholded map at $p = .05$. The cutoff value can be freely adjusted using the thresholding bar. Fig. 6B-C illustrates two example snapshots of visualizing mCC and cortical topographic maps.

Moreover, *CCmapping* also provides file-uploading services, which enable online estimation and visualization of topographic maps for a customized region of interest (ROI) on the mCC or cortical ROI. The customized ROI mask file could be uploaded to the upper right corner within the mCC or cortical surface panel. Fig. 6D-E illustrates mCC and cortical topographic maps for two example customized cortical or mCC ROIs.

Application of resultant topographic maps. To confirm whether positional dependence exists between the callosal axon and its connected cortical regions, we separately evaluated the correlation of the Y coordinates (i.e., the anterior-posterior direction) and Z coordinates (i.e., the dorsal-ventral direction) of mCC voxels with the barycenter of their connected cortical regions. Fig. 7A confirm that there is a significant correlation in both directions (Y coordinate: $r = .99$, $p < 0.001$; Z coordinate: $r = .96$, $p < 0.001$). These correlations indicate that 1) the callosal fibers passing through the anterior part of the mCC are more likely to connect the anterior cortical region and 2) the callosal fibers passing through the dorsal part of the mCC are more likely to connect the dorsal cortical region.

Next, to test whether the myelin content of parcellated cortical regions relates to the composition of their connected callosal fibers, we evaluated the correlation of the T1/T2 ratio values of cortical regions with the neurite density index (NDI) and orientation dispersion index (ODI) values of their passing mCC region (44). For all 4 cortical parcellations, significant negative correlations (all $ps < 0.05$) were observed for both NDI and ODI (Fig. 7B). Accordingly, more cortical myelin content is associated with less fiber density and orientational dispersion on the mCC. This result suggests a biological association between cortical myeloarchitecture and cortical information transfer to the other hemisphere.

Discussion

Using a high-quality diffusion MRI dataset from a large group of healthy adults we constructed the first bidirectional population-based connectional atlas between the mCC and cerebral cortex of the human brain. This comprehensive atlas provides connectional topographic maps for both the mCC and cortical surface at the highest resolution ever (i.e.,

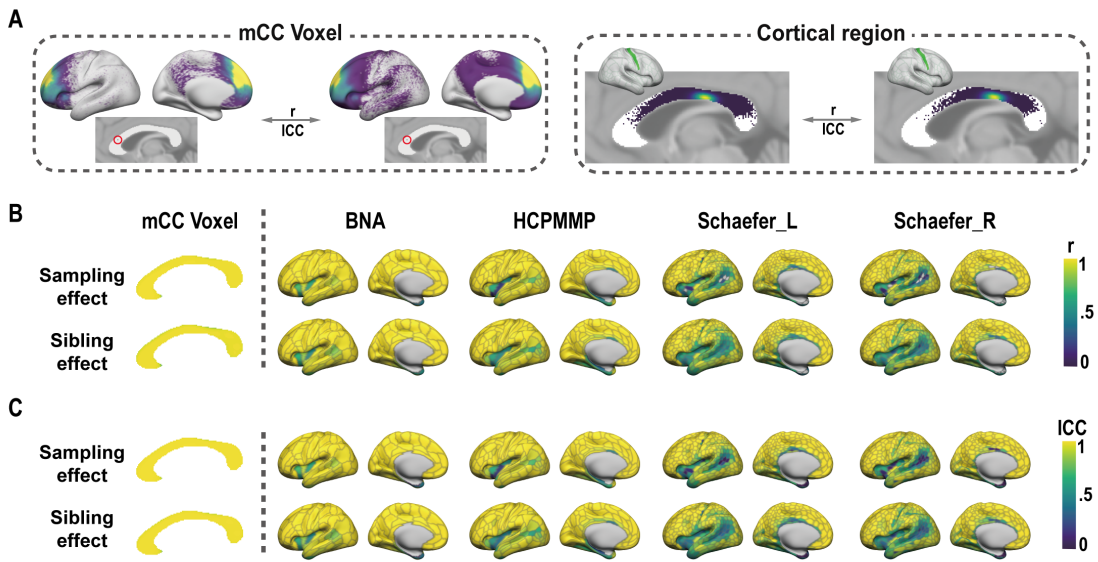


Fig. 4. Reproducibility of probability-weighted topographic maps: the sampling and sibling effects. (A) The schematics of measuring spatial similarity between two topographic maps. Left: measuring similarity between two cortical topographic maps for each mCC voxel. One example voxel (red circle) is selected, and its cortical topographic map is displayed. Right: measuring similarity between two mCC topographic maps for each pair of homotopic regions. One example cortical region (green) is selected, and its mCC topographic map is displayed. R: Pearson correlation; ICC: intraclass correlation. (B) The r-based similarity of topographic maps between two split-half HCP samples (i.e., the sampling effect, top row) and between unrelated and whole HCP samples (i.e., the sibling effect, bottom row). (C) The ICC-based similarity of topographic maps between two split-half HCP samples (i.e., the sampling effect, top row) and between unrelated and whole HCP samples (i.e., the sibling effect, bottom row). The relevant results for relative streamline number-weighted topographic maps are included in Figure S3.

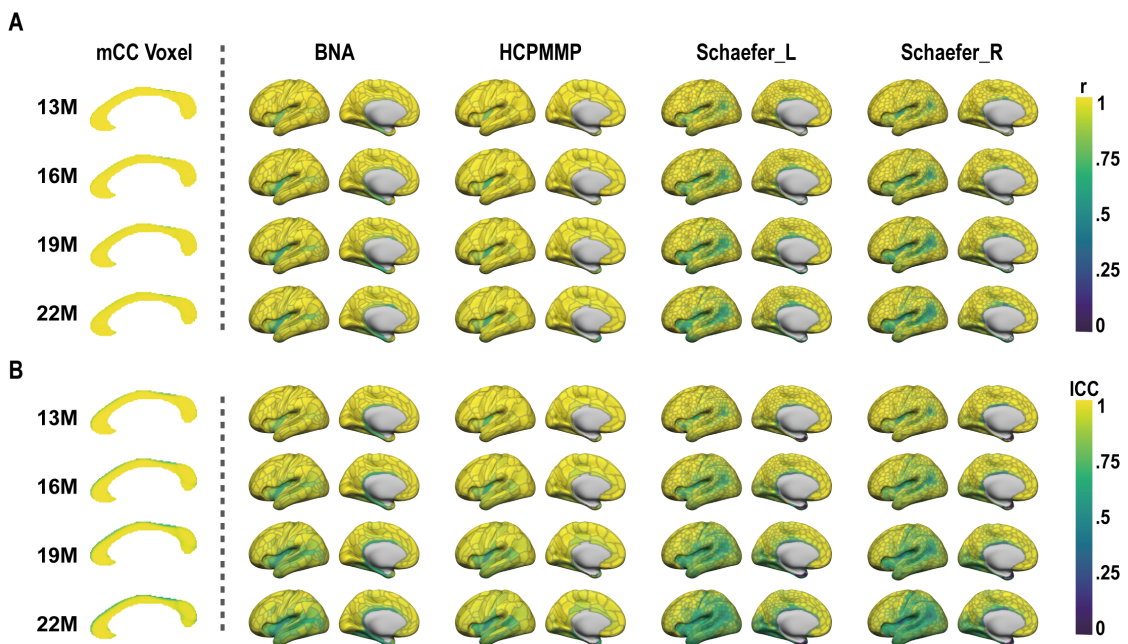


Fig. 5. Reproducibility of probability-weighted topographic maps: the effect of initially generated streamline number. (A) The r-based similarity of topographic maps between our main results from 10 M initially generated streamlines and others from more streamlines (i.e., 13 M, 16 M, 19 M, 22 M). (B) The ICC-based similarity of topographic maps between our main results from 10 M initially generated streamlines and others from more streamlines (i.e., 13 M, 16 M, 19 M, 22 M). The relevant results for relative streamline number-weighted topographic maps are included in Figure S4.

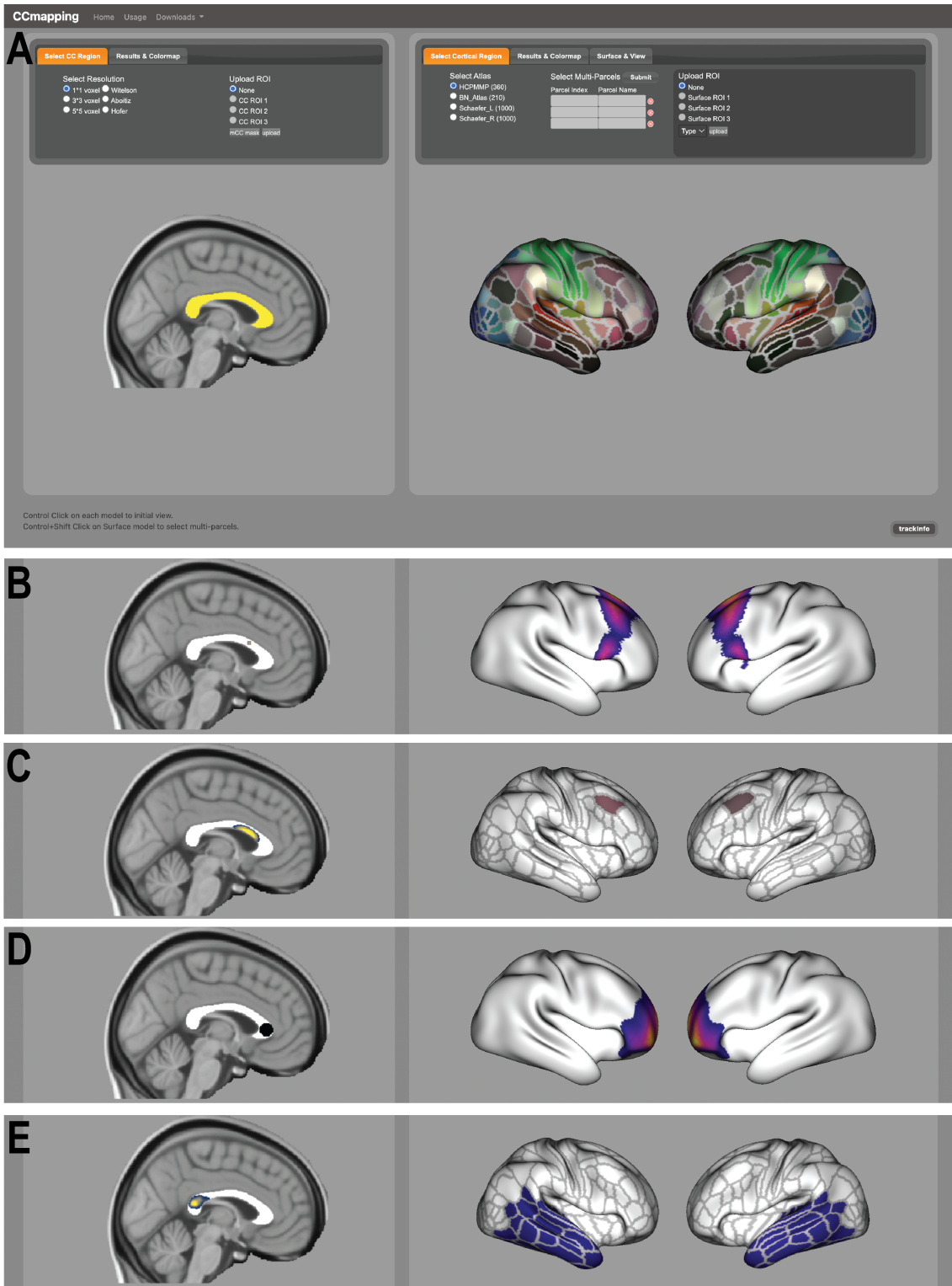


Fig. 6. CCmapping for visualizing cortical or mCC topographic maps. (A) The interface of CCmapping. (B) Snapshot visualizing the cortical topographic map for an example selected voxel on the mCC. (C) Snapshot visualizing the mCC topographic map for an example selected cortical region. (D) Snapshot visualizing the cortical topographic map for an example customized ROI on the mCC. (E) Snapshot visualizing the mCC topographic map for an example customized cortical ROI.

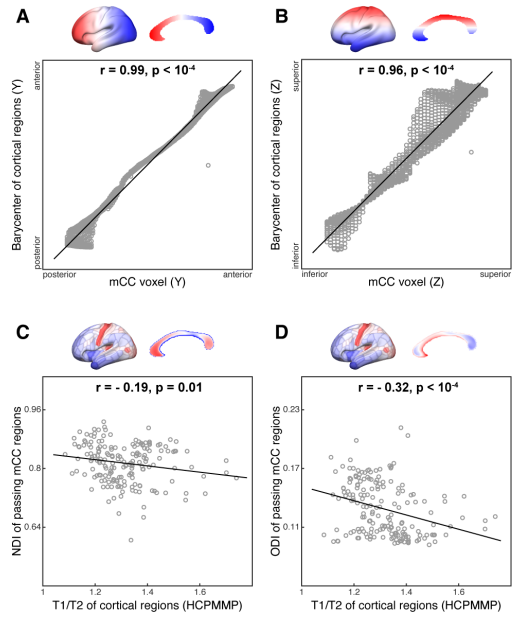


Fig. 7. Assessing relationships between callosal fibers and their connected cortical regions by population-based topographic maps. (A) The correlation of the Y and Z coordinates of mCC voxels with the barycenter of their connected cortical regions. The connected cortical region for each mCC voxel was derived from the thresholded mCC topographic map at $p = .05$. The Y and Z coordinates represent the relative positioning along the anterior-posterior (A-P) and dorsal-ventral (D-V) axes, respectively. (B) The correlation of the T1/T2 ratio values of cortical regions with the NDI and ODI values of their passing mCC region. The passing mCC region for each homotopic region pair was derived from the thresholded mCC topographic map at $p = .05$.

mCC voxel and small cortical patch). The validity and reproducibility of the estimated topographic maps were proven by comparisons with existing histological data and between population sampling, respectively. A user-friendly interactive online tool, i.e., CCmapping, was further developed for easily visualizing and accessing these maps. Through these topographic maps, preliminary analyses revealed positional dependence and microstructural correlations between callosal fibers and their connected cortical regions in the human brain, demonstrating the added value of these maps in understanding human callosal connections.

Mapping cortical topographies for mCC regions is fundamental for understanding functional relevance of white matter microstructures. As many reports show group differences in mCC regions, past studies chose to map observed clusters into Witelson or Hofer subdivisions and inferred connected cortical regions based on the corresponding subdivision (4, 6–8). However, for any predefined or observed cluster or region on the mCC that does not exactly match one entire subdivision, there have been no (even coarsely) summarized cortical connectional topographies available. These issues can be well addressed by our currently constructed callosal atlas, which offers pre-estimated cortical topographic maps at the mCC voxel level and is able to provide quantitative cortical topographies for any cluster or region on the mCC. Particularly, offering specific cortical maps for clusters or regions on the mCC enables quantitative in-house analyses

between mCC and cortical measures with the investigators' multimodal data, apart from simply inferring the function of the mCC cluster through its connected cortical regions.

Mapping topographies on the mCC for callosal fibers connecting different cortical regions helps understanding within-CC topographic organization. The mCC topographies for cortical regions have been applied to parcellate the entire mCC into subdivisions (10, 19, 20). To measure callosal fibers underlying visual and motor processing between the two hemispheres, previous studies have mapped the mCC topographies for the visual and motor areas (24–26). Moreover, a few studies have elegantly mapped the mCC topographies for all parcellated cortical regions from the entire cerebral cortex (21–23). The resultant mCC topographies in these studies, however, are limited by the low resolution of their cortical parcellations, i.e., too large a size for each cortical region (the maximum total number of cortical regions being less than 50). In contrast to these studies, our currently constructed callosal atlas offers detailed mCC topographies for cortical parcellations at much higher resolution, i.e., 105 BNA-based cortical regions, 180 HCPMMP-based cortical regions, 500 Schaefer_L-based cortical regions, and 498 Schaefer_R-based cortical regions, improving the applicability of mCC topographic maps. Such advanced CC mapping will permit quantitative in-house analyses between mCC and cortical measures with more precision and flexibility.

The estimated topographic maps are consistent with existing histological data in the literature (i.e., the gold standard available). Such validity likely relates to our state-of-the-art diffusion MRI acquisition and tractography, as well as the population-based nature of these maps. Additionally, the ultimate topographic maps were generated by combining individual tractography data from almost 1000 healthy adults. The combination across such a large group of healthy adults can effectively reduce noises or errors that occur randomly at the individual level, further improving the accuracy of the ultimate topographic maps.

The callosal connectional reproducibility of the temporal and insular lobes was relatively low comparing to other regions (Fig 5). This might relate to lower density of callosal fiber reaching the temporal and insula lobes. Previous studies have shown that anatomical connection strength decays exponentially with connectional length across the entire brain (45). Given the relatively greater length of callosal fibers connecting the temporal and insula lobe than the other lobes (46), the lower density of callosal fibers reaching the temporal lobe is to some extent expected. Such lower interhemispheric connectional density might be compensated by the axon fibers connecting bilateral temporal cortices through the anterior commissure (16, 46). On the other hand, the intrinsic technical limitation of dMRI tractography in reconstructing crossing fibers could partly contribute to the observed lower reproducibility around the temporal and insular lobes, although the current study did try to minimize the tractography errors by employing high-angular resolution dMRI data, cutting-edge local orientation modeling, sophisticated tractography algorithms, and post fiber filtering process (30, 34, 47). Con-

sidering that some callosal fibers are severely crossed by the central white matter “periventricular crossroads” (e.g., intersecting callosal, associative and thalamocortical fibers), our tractography may fail to or less robustly find callosal fibers connecting bilateral temporal and insular lobes due to some algorithm errors. Therefore, the interpretation of callosal connectional topographic maps for these temporal and insular regions should be cautious.

The present study offers efficient solutions for two key issues of usability: 1) thresholding and 2) accessing these maps. First, rigorously thresholding a brain map is often required before analyses and interpretation. Numerous thresholding methods have been developed for statistical parametric maps (e.g., t map, p map) (48, 49). However, they are not suitable for our data. Therefore, an in-house thresholding method based on permutation and Moran spectral randomization was developed (39), which should be usable for other studies with similar data structures. Using this method, a threshold value at the statistical significance level of $p = 0.05$ was estimated and saved for each mCC or cortical topographic map. Through the statistically meaningful topographic boundary or mask on the thresholded maps, the topography-based analysis and interpretation are greatly facilitated. Second, viewing and accessing the estimated topographic maps is also challenging, as the entire atlas includes thousands of cortical or mCC topographic maps, each linking to a selected mCC voxel/subdivision or cortical region. Given the complex data correspondence, simultaneously showing the selected mCC voxel/subdivision or cortical region as well as its linked topographic map is essential for efficient viewing. Our solution for this is CCmapping, an online tool that was exclusively developed for visualizing and exporting the estimated topographic maps. Particularly, the CCmapping has prestored the estimated threshold values for all maps and the enormous amount of map files on the cloud. This allows for an interactive view of requested topographic maps in a modern web browser after quickly loading them from the cloud, a useful function for both research and educational purposes. Moreover, CCmapping supports exporting the loaded topographic maps to local files, enabling in-house analyses with specific topographic maps. Taken together, the two solutions above effectively boost the usability and accessibility of our atlas.

Previous studies have shown dorsal-ventral positional dependence for the specific local part of the CC (25, 42). Our findings replicated this positional dependence and extended this organizational principle to the entire human CC. Such organization minimizes the overall callosal fiber length, therefore supporting the optimal wiring hypothesis for the brain organization (50, 51). Additionally, this positional dependence is compatible with the notion that neuronal axons within each WM tract are positioned in an orderly manner in terms of their origination (41, 42). Moreover, this atlas revealed an association of callosal fiber microstructures with their connected cortical regions. Such an association further confirms a biological link between cortical myeloarchitecture and its information transfer to the other hemisphere (29): sensorimotor cortices contain more myelin and communicate with

the contralateral hemisphere by callosal fibers with larger diameters; association cortices contain less myelin and communicate with the contralateral hemisphere by callosal fibers with smaller diameters. Future investigation is warranted to determine the functional mechanisms underlying this link. Finally, a few limitations should be addressed. First, the validation for our topographic maps is based on the histological data in the literature. These data are limited and describe relatively coarse anatomical locations, leading to our validation analysis at a very low resolution. Next, our estimated maps were derived from healthy young adults with twins. Typically, twins have a higher incidence of premature birth that is associated with a thinning of specific mCC regions (52), therefore could confound the topographic maps to some degree. It is unclear whether the currently estimated maps based on the HCP young adults can be extrapolated to other populations (e.g., newborns and patients with brain diseases). Future studies are encouraged to map topographic maps for other populations and even other species (e.g., macaque). Next, our current callosal connectional maps were based on young adults, maintaining a balanced representation of males and females. It should be noted that both age and sex have nontrivial influence on the CC morphology and microstructure. For example, the CC volume and fractional anisotropy (FA) were found to increase during childhood and adolescence, peak in young adulthood, and then decrease in elderly (53, 54). The mean magnetization transfer ratio (MTR) of the CC showed significant sex difference: a higher myelin content per unit of white matter tissue in young men than women (55). Future studies are warranted to elucidate the role of age and sex on the callosal connectional topographic maps. In addition to the population-based atlas, individualized topographic maps are of great value for personalized analysis and interpretation but are beyond the scope of our current study. In future studies, the currently generated atlas can be taken as an initial point for accurately estimating the callosal connectional topographies at the individual level.

Literature	Species	Trace injection site	Reported connectional position	Consistency with our results
(11)	Macaca	frontal occipital parietal and temporal	the genu and anterior third of the body splenium and posterior third of the body (isthmus) posterior two-thirds of the body (isthmus)	✓ ✓ ✓
(12)	Macaca mulatta	rostral half caudal half splenium midline in the posterior half caudal part of the body	frontal lobe parietal, temporal and occipital lobe and insulo-opercular region occipital lobe and prostriate area precentral opercula temporal lobe	✓ ✓ ✓ ✓ ✓
(13)	Macaca mulatta	prelunate gyri	splenium	✓
(14)	Macaca mulatta	area 46 area 25 and 32 area 13 and 14 area 8 area 46v and area 12	genu and anterior body genu anterior portion of the genu, and the rostrum the border of the genu and the body genu	✓ ✓ ✓ ✓ ✓
(16)	Macaca mulatta	paAlt and Ts3	rostral to splenium	✓
(17)	Macaca mulatta	area 18 area 19	posterior 3-4 mm of the splenium splenium, dorsal to area 18	✓ ✓
(56)	Macaca fascicularis	area 9 and 9/46 border area 6 and F4 area 4 area 2 area 5 areas 17 and 18	genu anterior part of body posterior part of body isthmus posterior part of isthmus and splenium posterior part of splenium	✓ ✓ ✓ ✓ ✓ ✓
(18)	Human	inferior frontal and anterior inferior parietal posterior superior frontal temporo-parieto-occipital junction superior parietal region occipital lobe region mid-temporal region	genu body splenium splenium splenium anterior body	✓ ✓ ✓ ✓ ✓ ✓

Table 1. Comparison of existing histological monkey or human mapping results of callosal connections with our currently estimated population-based topographic results.

CONFLICTS OF INTERESTS

The authors have no conflicts of interest to declare.

ACKNOWLEDGEMENTS

This work was supported by the China Brain Initiative (grant 2021ZD0201701, 2021ZD0200502, G.G.) and National Science Foundation of China (82172016, G.G.). Data were provided by the Human Connectome Project, WU-Minn Consortium (Principal Investigators: David Van Essen and Kamil Ugurbil; 1U54MH091657) funded by the 16 NIH Institutes and Centers that support the NIH reprint for Neuroscience Research; and by the McDonnell Center for Systems Neuroscience at Washington University.

Bibliography

1. Michael S. Gazzaniga. Cerebral specialization and interhemispheric communication Does the corpus callosum enable the human condition? *Brain*, 123(7):1293–1326, July 2000. ISSN 0006-8950. doi: 10.1093/brain/123.7.1293.
2. Goulven Josse, Mohamed L. Seghier, Ferath Kherif, and Cathy J. Price. Explaining Function with Anatomy: Language Lateralization and Corpus Callosum Size. *Journal of Neuroscience*, 28(52):14132–14139, December 2008. ISSN 0270-6474, 1529-2401. doi: 10.1523/JNEUROSCI.4383-08.2008.
3. Eileen Luders, Paul M. Thompson, Katherine L. Narr, Alen Zamanyan, Yi-Yu Chou, Boris Gutman, Ivo D. Dinov, and Arthur W. Toga. The link between callosal thickness and intelligence in healthy children and adolescents. *NeuroImage*, 54(3):1823–1830, February 2011. ISSN 1053-8119. doi: 10.1016/j.neuroimage.2010.09.083.
4. Jason J. Wolff, Guido Gerig, John D. Lewis, Takahiro Soda, Martin A. Styner, Clement Vachet, Kelly N. Botteron, Jed T. Elison, Stephen R. Dager, Annette M. Estes, Heather C. Hazlett, Robert T. Schultz, Lonnie Zwagbaum, Joseph Piven, and IBIS Network. Altered corpus callosum morphology associated with autism over the first 2 years of life. *Brain: A Journal of Neurology*, 138(Pt 7):2046–2058, July 2015. ISSN 1460-2156. doi: 10.1093/brain/awv118.
5. Qiyun Fan, Qiyuan Tian, Ned A. Ohringer, Aapo Nummenmaa, Thomas Witzel, Sean M. Tobey, Eric C. Klawiter, Choukri Mekkaoui, Bruce R. Rosen, Lawrence L. Wald, David H. Salat, and Susie Y. Huang. Age-related alterations in axonal microstructure in the corpus callosum measured by high-gradient diffusion MRI. *NeuroImage*, 191:325–336, May 2019. ISSN 1053-8119. doi: 10.1016/j.neuroimage.2019.02.036.
6. H. Diana Rosas, Stephanie Y. Lee, Alexander C. Bender, Alexandra K. Zaleta, Mark Vangel, Peng Yu, Bruce Fischl, Vasanth Pappu, Christina Onorato, Jang-Ho Cha, David H. Salat, and Steven M. Hersch. Altered white matter microstructure in the corpus callosum in Huntington's disease: Implications for cortical "disconnection". *NeuroImage*, 49(4):2995–3004, February 2010. ISSN 1053-8119. doi: 10.1016/j.neuroimage.2009.10.015.
7. Jian Li, Elliot Kaled Edmiston, Kaiyuan Chen, Yaqing Tang, Xuan Ouyang, Yifeng Jiang, Guoguang Fan, Ling Ren, Jie Liu, Yifang Zhou, Wenyan Jiang, Zhenning Liu, Ke Xu, and Fei Wang. A comparative diffusion tensor imaging study of corpus callosum subregion integrity in bipolar disorder and schizophrenia. *Psychiatry Research: Neuroimaging*, 221(1):58–62, January 2014. ISSN 0925-4927. doi: 10.1016/j.psychresns.2013.10.007.
8. Ian O. Bledsoe, Glenn T. Stebbins, Doug Merkitch, and Jennifer G. Goldman. White matter abnormalities in the corpus callosum with cognitive impairment in Parkinson disease. *Neurology*, 91(24):e2244–e2255, December 2018. ISSN 1526-632X. doi: 10.1212/WNL.0000000000006646.
9. S. F. Witelson. Hand and sex differences in the isthmus and genu of the human corpus callosum. A postmortem morphological study. *Brain: A Journal of Neurology*, 112 (Pt 3): 799–835, June 1989. ISSN 0006-8950. doi: 10.1093/brain/112.3.799.
10. Sabine Hofer and Jens Frahm. Topography of the human corpus callosum revisited—Comprehensive fiber tractography using diffusion tensor magnetic resonance imaging. *NeuroImage*, 32(3):989–994, September 2006. ISSN 1053-8119. doi: 10/fm9pnf.
11. S. Sunderland. THE DISTRIBUTION OF COMMISSURAL FIBRES IN THE CORPUS CALLOSUM IN THE MACAQUE MONKEY. *Journal of Neurology and Psychiatry*, 3(1):9–18, January 1940. ISSN 0368-329X.
12. D. N. Pandya, E. A. Karol, and D. Heilbronn. The topographical distribution of interhemispheric projections in the corpus callosum of the rhesus monkey. *Brain Research*, 32(1): 31–43, September 1971. ISSN 0006-8993. doi: 10.1016/0006-8993(71)90153-3.
13. H. A. Swadlow, D. L. Rosene, and S. G. Waxman. Characteristics of interhemispheric impulse conduction between prelunate gyri of the rhesus monkey. *Experimental Brain Research*, 33(3):455–467, September 1978. ISSN 1432-1106. doi: 10.1007/BF00235567.
14. H. Barbas and D. N. Pandya. Topography of commissural fibers of the prefrontal cortex in the rhesus monkey. *Experimental Brain Research*, 55(1):187–191, May 1984. ISSN 1432-1106. doi: 10.1007/BF00240516.
15. Giorgio M. Innocenti, Kerstin Schmidt, Chantal Milleret, Mara Fabri, Maria G. Knyazeva, Alexandra Battaglia-Mayer, Francisco Abolitz, Maurice Pitti, Matteo Caleo, Carlo A. Marzi, Muhammed Barakovic, Franco Lepore, and Roberto Caminiti. The functional characterization of callosal connections. *Progress in Neurobiology*, 208:102186, January 2022. ISSN 0301-0082. doi: 10.1016/j.pneurobio.2021.102186.
16. P. B. Cipolloni and D. N. Pandya. Topography and trajectories of commissural fibers of the superior temporal region in the rhesus monkey. *Experimental Brain Research*, 57(2): 381–389, January 1985. ISSN 1432-1106. doi: 10.1007/BF00236544.
17. K. S. Rockland and D. N. Pandya. Topography of occipital lobe commissural connections in the rhesus monkey. *Brain Research*, 365(1):174–178, February 1986. ISSN 0006-8993. doi: 10.1016/0006-8993(86)90736-5.
18. M. C. de Lacoste, J. B. Kirkpatrick, and E. D. Ross. Topography of the human corpus callosum. *Journal of Neuropathology and Experimental Neurology*, 44(6):578–591, November 1985. ISSN 0022-3069. doi: 10/c7ph66.
19. Hao Huang, Jiangyang Zhang, Hangyi Jiang, Setsu Wakana, Lidia Poetscher, Michael I. Miller, Peter CM. van Zijl, Argye E. Hillis, Robert Wykik, and Susumu Mori. DTI tractography based parcellation of white matter: Application to the mid-sagittal morphology of corpus callosum. *NeuroImage*, 26(1):195–205, May 2005. ISSN 1053-8119. doi: 10/ck6ppj.
20. Mojtaba Zarei, Heidi Johansen-Berg, Steve Smith, Olga Ciccarelli, Alan J. Thompson, and Paul M. Matthews. Functional anatomy of interhemispheric cortical connections in the human brain. *Journal of Anatomy*, 209(3):311–320, September 2006. ISSN 0021-8782. doi: 10.1111/j.1469-7580.2006.00615.x.
21. Hae-Jeong Park, Jae Jin Kim, Seung-Koo Lee, Jeong Ho Seok, Jiwon Chun, Dong Ik Kim, and Jong Doo Lee. Corpus callosum connection mapping using cortical gray matter parcellation and DT-MRI. *Human Brain Mapping*, 29(5):503–516, 2008. ISSN 1097-0193. doi: 10.1002/hbm.20314.
22. Yi-Ping Chao, Kuan-Hung Cho, Chun-Hung Yeh, Kun-Hsien Chou, Jyh-Horng Chen, and Ching-Po Lin. Probabilistic topography of human corpus callosum using cytoarchitectural parcellation and high angular resolution diffusion imaging tractography. *Human Brain Mapping*, 30(10):3172–3187, October 2009. ISSN 1097-0193. doi: 10/c9tmf4.
23. Kerstin Pannek, Jane L. Mathias, Erin D. Bigler, Greg Brown, Jamie D. Taylor, and Stephen Rose. An automated strategy for the delineation and parcellation of commissural pathways suitable for clinical populations utilising high angular resolution diffusion imaging tractography. *NeuroImage*, 50(3):1044–1053, April 2010. ISSN 1053-8119. doi: 10/cfpmv.
24. Robert F. Dougherty, Michal Ben-Shachar, Roland Bammer, Alyssa A. Brewer, and Brian A. Wandell. Functional organization of human occipital-callosal fiber tracts. *Proceedings of the National Academy of Sciences of the United States of America*, 102(20):7350–7355, May 2005. ISSN 0027-8424. doi: 10.1073/pnas.0500003102.
25. Mathias Wahl, Birgit Lauterbach-Soon, Elke Hattingen, Patrick Jung, Oliver Singer, Steffen Volz, Johannes C. Klein, Helmuth Steinmetz, and Ulf Ziemann. Human Motor Corpus Callosum: Topography, Somatotopy, and Link between Microstructure and Function. *Journal of Neuroscience*, 27(45):12132–12138, November 2007. ISSN 0270-6474, 1529-2401. doi: 10.1523/JNEUROSCI.1230-07.2007.
26. M. Saenz and I. Fine. Topographic organization of V1 projections through the corpus callosum in humans. *NeuroImage*, 52(4):1224–1229, October 2010. ISSN 1095-9572. doi: 10/dq954w.
27. D. C. Van Essen, K. Ugurbil, E. Auerbach, D. Barch, T. E. J. Behrens, R. Bucholz, A. Chang, L. Chen, M. Corbetta, S. W. Curtiss, S. Della Penna, D. Feinberg, M. F. Glasser, N. Harel, A. C. Heath, L. Larson-Prior, D. Marcus, G. Michalareas, S. Moeller, R. Oostenveld, S. E. Petersen, F. Prior, B. L. Schlaggar, S. M. Smith, A. Z. Snyder, J. Xu, and E. Yacoub. The Human Connectome Project: A data acquisition perspective. *NeuroImage*, 62(4):2222–2231, October 2012. ISSN 1095-9572 1053-8119. doi: 10/gf268v.
28. Matthew F. Glasser and David C. Van Essen. Mapping human cortical areas in vivo based on myelin content as revealed by T1- and T2-weighted MRI. *The Journal of Neuroscience: The Official Journal of the Society for Neuroscience*, 31(32):11597–11616, August 2011. ISSN 1529-2401. doi: 10.1523/JNEUROSCI.2180-11.2011.
29. Liyuan Yang, Chenxi Zhao, Yirong Xiong, Suyu Zhong, Di Wu, Shaoling Peng, Michel Thiebaut de Schotten, and Gaolang Gong. Callosal fiber length scales with brain size according to functional lateralization, evolution, and development. *Journal of Neuroscience*, March 2022. ISSN 0270-6474, 1529-2401. doi: 10.1523/JNEUROSCI.1510-21.2022.
30. J.-Donald Tournier, Fernando Calamante, and Alan Connelly. Robust determination of the fibre orientation distribution in diffusion MRI: Non-negativity constrained super-resolved spherical deconvolution. *NeuroImage*, 35(4):1459–1472, May 2007. ISSN 1053-8119. doi: 10/drdc5b.
31. Ben Jeurissen, Jacques-Donald Tournier, Thijs Dhollander, Alan Connelly, and Jan Sijbers. Multi-tissue constrained spherical deconvolution for improved analysis of multi-shell diffusion MRI data. *NeuroImage*, 103:411–426, December 2014. ISSN 1095-9572 1053-8119. doi: 10/f6rb29.
32. J.-Donald Tournier, Robert Smith, David Raffelt, Rami Tabbara, Thijs Dhollander, Maximilian Pietsch, Daan Christiaens, Ben Jeurissen, Chun-Hung Yeh, and Alan Connelly. MRtrix3: A fast, flexible and open software framework for medical image processing and visualisation. *NeuroImage*, 202:116137, November 2019. ISSN 1095-9572 1053-8119. doi: 10/ggtbms.
33. Stephen M. Smith, Mark Jenkinson, Mark W. Woolrich, Christian F. Beckmann, Timothy E. J. Behrens, Heidi Johansen-Berg, Peter R. Bannister, Marilena De Luca, Ivana Dobrota, David E. Flitney, Rami K. Niazy, James Saunders, John Vickers, Yongyue Zhang, Nicola De Stefano, J. Michael Brady, and Paul M. Matthews. Advances in functional and structural MR image analysis and implementation as FSL. *NeuroImage*, 23:S208–S219, 2004/01/01. ISSN 1053-8119. doi: 10/cbsrtg.
34. R. E. Smith, J. D. Tournier, F. Calamante, and A. Connelly. Anatomically-constrained tractography: Improved diffusion MRI streamlines tractography through effective use of anatomical information. *NeuroImage*, 62(3):1924–38, September 2012. ISSN 1095-9572 (Electronic) 1053-8119 (Linking). doi: 10/f364bh.
35. F. Abotiz, A. B. Scheibel, R. S. Fisher, and E. Zaidel. Fiber Composition of the Human Corpus Callosum. *Brain Research*, 598(1-2):143–153, December 1992. ISSN 0006-8993. doi: 10/b4qh38.
36. Lingzhong Fan, Hai Li, Junjie Zhuo, Yu Zhang, Jiaoqian Wang, Liangfu Chen, Zhengyi Yang, Congying Chu, Sangma Xie, Angela R. Laird, Peter T. Fox, Simon B. Eickhoff, Chunshui Yu, and Tianzi Jiang. The Human Brainnetome Atlas: A New Brain Atlas Based on Connectional Architecture. *Cerebral Cortex*, 26(8):3508–3526, August 2016. ISSN 1047-3211. doi: 10.1093/cercor/bhw157.
37. Matthew F. Glasser, Timothy S. Coalson, Emma C. Robinson, Carl D. Hacker, John Harwell, Essa Yacoub, Kamil Ugurbil, Jesper Andersson, Christian F. Beckmann, Mark Jenkinson, Stephen M. Smith, and David C. Van Essen. A multi-modal parcellation of human cerebral cortex. *Nature*, 536(7615):171–178, August 2016. ISSN 1476-4687. doi: 10.1038/nature18933.
38. Alexander Schaefer, Ru Kong, Evan M Gordon, Timothy O Laumann, Xi-Nian Zuo, Avram J Holmes, Simon B Eickhoff, and B T Thomas Yeo. Local-Global Parcellation of the Human Cerebral Cortex from Intrinsic Functional Connectivity MRI. *Cerebral Cortex*, 28(9):3095–3114, September 2018. ISSN 1047-3211. doi: 10.1093/cercor/bhx179.
39. Reinder Vos de Wael, Oualid Benkarim, Casey Paquola, Sara Lariviere, Jessica Royer, Shahin Tavakol, Ting Xu, Seok-Jun Hong, Georg Langs, Sofie Valk, Bratislav Misic, Michael Milham, Daniel Margulies, Jonathan Smallwood, and Boris C. Bernhardt. BrainSpace:

- A toolbox for the analysis of macroscale gradients in neuroimaging and connectomics datasets. *Communications Biology*, 3(1):1–10, March 2020. ISSN 2399-3642. doi: 10.1038/s42003-020-0794-7.
40. Tarek Sherif, Nicolas Kassis, Marc-Étienne Rousseau, Reza Adalat, and Alan C. Evans. BrainBrowser: Distributed, web-based neurological data visualization. *Frontiers in Neuroinformatics*, 8:89, 2015. ISSN 1662-5196. doi: 10.3389/fninf.2014.00089.
 41. Van J. Wedeen, Douglas L. Rosene, Ruopeng Wang, Guangping Dai, Farzad Mortazavi, Patrik Hagmann, Jon H. Kaas, and Wen-Yih I. Tseng. The Geometric Structure of the Brain Fiber Pathways. *Science*, 335(6076):1628–1634, March 2012. doi: 10.1126/science.1215280.
 42. Jing Zhou, Yunqing Wen, Liang She, Ya-nan Sui, Lu Liu, Linda J. Richards, and Mu-ming Poo. Axon position within the corpus callosum determines contralateral cortical projection. *Proceedings of the National Academy of Sciences*, 110(29):E2714–E2723, July 2013. doi: 10.1073/pnas.1310233110.
 43. Matthew F. Glasser, Timothy S. Coalson, Michael P. Harms, Junqian Xu, Graham L. Baum, Joonas A. Autio, Edward J. Auerbach, Douglas N. Greve, Essa Yacoub, David C. Van Essen, Nicholas A. Bock, and Takuya Hayashi. Empirical transmit field bias correction of T1w/T2w myelin maps. *NeuroImage*, 258:119360, September 2022. ISSN 1053-8119. doi: 10.1016/j.neuroimage.2022.119360.
 44. Hui Zhang, Torben Schneider, Claudia A. Wheeler-Kingshott, and Daniel C. Alexander. NODDI: Practical in vivo neurite orientation dispersion and density imaging of the human brain. *NeuroImage*, 61(4):1000–1016, 2012/07/16/. ISSN 1053-8119. doi: 10.1016/j.neuroimage.2012.03.072.
 45. Mária Ercsey-Ravasz, Nikola T. Markov, Camille Lamy, David C. Van Essen, Kenneth Knoblauch, Zoltán Toroczkai, and Henry Kennedy. A predictive network model of cerebral cortical connectivity based on a distance rule. *Neuron*, 80(1):184–197, 2013. ISSN 0896-6273. doi: <https://doi.org/10.1016/j.neuron.2013.07.036>.
 46. Abhidha Shah, Sukhdeep Jhawar, Aimee Goel, and Atul Goel. Corpus callosum and its connections: A fiber dissection study. *World Neurosurgery*, 151:e1024–e1035, 2021. ISSN 1878-8750. doi: <https://doi.org/10.1016/j.wneu.2021.05.047>.
 47. R. E. Smith, J. D. Tournier, F. Calamante, and A. Connolly. SIFT: Spherical-deconvolution informed filtering of tractograms. *NeuroImage*, 67:298–312, February 2013. ISSN 1095-9572 (Electronic) 1053-8119 (Linking). doi: 10.1016/j.neuroimage.2012.11.049.
 48. K. J. Friston, A. P. Holmes, K. J. Worsley, J.-P. Poline, C. D. Frith, and R. S. J. Frackowiak. Statistical parametric maps in functional imaging: A general linear approach. *Human Brain Mapping*, 2(4):189–210, 1994. ISSN 1097-0193. doi: 10.1002/hbm.460020402.
 49. Choong-Wan Woo, Anjali Krishnan, and Tor D. Wager. Cluster-extent based thresholding in fMRI analyses: Pitfalls and recommendations. *NeuroImage*, 91:412–419, May 2014. ISSN 1053-8119. doi: 10.1016/j.neuroimage.2013.12.058.
 50. Dmitri B. Chklovskii, Thomas Schikorski, and Charles F. Stevens. Wiring Optimization in Cortical Circuits. *Neuron*, 34(3):341–347, April 2002. ISSN 0896-6273. doi: 10.1016/S0896-6273(02)00679-7.
 51. Fernanda Tovar-Moll, Myriam Monteiro, Juliana Andrade, Ivanei E. Bramati, Rodrigo Vianna-Barbosa, Theo Marins, Erika Rodrigues, Natalia Dantas, Timothy E. J. Behrens, Ricardo de Oliveira-Souza, Jorge Moll, and Roberto Lent. Structural and functional brain rewiring clarifies preserved interhemispheric transfer in humans born without the corpus callosum. *Proceedings of the National Academy of Sciences*, 111(21):7843–7848, May 2014. doi: 10.1073/pnas.1400806111.
 52. Chiara Nosarti, Teresa M. Rushe, Peter W. R. Woodruff, Ann L. Stewart, Larry Rifkin, and Robin M. Murray. Corpus callosum size and very preterm birth: relationship to neuropsychological outcome. *Brain*, 127(9):2080–2089, 08 2004. ISSN 0006-8950. doi: 10.1093/brain/awh230.
 53. Miho Ota, Takayuki Obata, Yoshihide Akine, Hiroshi Ito, Hiroo Ikehira, Takashi Asada, and Tetsuya Suhara. Age-related degeneration of corpus callosum measured with diffusion tensor imaging. *NeuroImage*, 31(4):1445–1452, 2006. ISSN 1053-8119. doi: <https://doi.org/10.1016/j.neuroimage.2006.02.008>.
 54. Nicole C.R. McLaughlin, Robert H. Paul, Stuart M. Grieve, Leanne M. Williams, David Laidlaw, Margaret DiCarlo, C. Richard Clark, William Whelihan, Ronald A. Cohen, Thomas J. Whitford, and Evian Gordon. Diffusion tensor imaging of the corpus callosum: a cross-sectional study across the lifespan. *International Journal of Developmental Neuroscience*, 25(4):215–221, 2007. ISSN 0736-5748. doi: <https://doi.org/10.1016/j.ijdevneu.2007.03.008>.
 55. L. Björnholm, J. Nikkinen, V. Kviniemi, T. Nordström, S. Niemelä, M. Drakesmith, JC Evans, GB Pike, J. Veijola, and T. Paus. Structural properties of the human corpus callosum: Multimodal assessment and sex differences. *NeuroImage*, 152:108–118, 2017. ISSN 1053-8119. doi: <https://doi.org/10.1016/j.neuroimage.2017.02.056>.
 56. Roberto Caminiti, Hassan Ghaziri, Ralf Galuske, Patrick R. Hof, and Giorgio M. Innocenti. Evolution amplified processing with temporally dispersed slow neuronal connectivity in primates. *Proceedings of the National Academy of Sciences of the United States of America*, 106(46):19551–19556, November 2009. ISSN 1091-6490. doi: 10.1073/pnas.0907655106.